28GHz Compact Omni-Directional Circularly Polarized Antenna for Device-to-Device (D2D) Communications in Future 5G Systems

Wei Lin, *Member, IEEE,* Richard W. Ziolkowski, *Fellow, IEEE* and Thomas C. Baum, *Member, IEEE*

***Abstract* — An omni-directional circularly polarized (OCP) antenna operating at 28GHz is reported and has been found to be a promising candidate for Device-to-Device (D2D) communications in the next generation (5G) wireless systems. The OCP radiation is realized by systematically integrating electric and magnetic dipole elements into a compact disc-shaped configuration (9.23 mm^3 = 0.0076 λ_0^3 at 28 GHz) in such a manner that they are oriented in parallel and radiate with the proper phase difference. The entire antenna structure was printed on a single piece of dielectric substrate using standard PCB manufacturing technologies and, hence, is amenable to mass production. A prototype OCP was fabricated on Rogers™ 5880 substrate and was tested. The measured results are in good agreement with their simulated values and confirm the reported design concepts. Good OCP radiation patterns were produced with a measured peak realized RHCP gain of 2.2 dBic. The measured OCP overlapped impedance & AR bandwidth was 2.2 GHz, from 26.5 to 28.7 GHz, an 8.0% fractional bandwidth, which completely covers the 27.5 to 28.35 GHz band proposed for 5G cellular systems.**

***Index Terms* — Circular polarization, compact antenna, Device-to-Device (D2D) communications, omni-directional patterns, 5G wireless systems**

I. Introduction

The next generation (5G) cellular mobile communication networks have undergone extensive conceptual development over the past few years. Operators envision that it will be commercially viable for the opening of the Tokyo 2020 Olympic Games. One evolutionary technology in 5G cellular systems is anticipated to be the use of the millimeter (mm-Wave) frequency spectrum to realize the high data rates and system capacities that have been forecast to meet the ever-growing performance demands of consumers. Experimental results have proved that the 28 GHz frequency band is suitable for such 5G mm-Wave cellular systems [1]. Specifically, the Federal Communications Commission (FCC) of the US has recently (July 2016) designated the frequency band from 27.5 to 28.35 GHz for 5G applications [2]. Another 5G breakthrough concept is the introduction of Device-to-Device (D2D) communications. D2D connectivity will bring significant improvements in system capacity, spectral efficiency, communication range, and channel reliability because it enables the realization of spatial diversity [3]. It necessitates that all portable wireless devices must be capable of communicating with any other nearby devices. It is an exciting and innovative feature expected for 5G networks.

These two evolutionary technologies for future 5G mobile terminals engender substantial challenges for their antenna systems. Conventional antennas in portable devices, such as those found in current smart phones, are not suitable for these 5G higher frequencies and their anticipated smaller sizes. To meet the anticipated design specifications for D2D communications at 28 GHz in 5G cellular systems, antennas must be developed that will generate circularly polarized (CP) fields with omni-directional radiation patterns as illustrated in the application diagram shown in Figure 1.

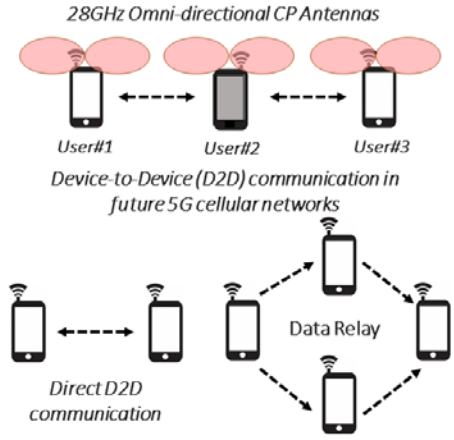

Fig. 1. Device-to-Device (D2D) application diagram for 28GHz

Manuscript received on May 21, 2017; revised on August 23, 2017; accepted on October 1 2017.

This work was supported in part by the Australian Research Council grant number DP160102219.

Wei Lin is with the University of Technology Sydney, Global Big Data Technologies Centre, Ultimo NSW 2007, Australia, (E-mail: wei.lin@uts.edu.au).

Richard. W. Ziolkowski is with the University of Technology Sydney, Global Big Data Technologies Centre, Ultimo NSW 2007, Australia, and the Department of Electrical and Computer Engineering, University of Arizona, Tucson, AZ 85721, USA (E-mail: Richard.Ziolkowski@uts.edu.au).

T. C. Baum is with the School of Electrical and Computer Engineering, Royal Melbourne Institute of Technology (RMIT University), Melbourne, Victoria, Australia, 3001 (e-mail: thomas.baum@rmit.edu.au)

omni-directional CP antennas anticipated for applications in 5G wireless systems.

Omni-directional CP (OCP) antennas with lower gain are expected to be the most suitable candidates for D2D applications in 5G wireless systems. They have much larger radiation coverage and, hence, enable diverse communication links among multi-users. It is noted that several initial studies on the basic operational needs for long distance 5G millimeter-wave communications have been performed [4]-[6]. They have demonstrated that high gain 28 GHz antenna arrays with highly directional beams will be required for those applications. On the other hand, it has also been confirmed that lower gain TX-RX systems will be sufficient for shorter communication distances such as those associated with D2D applications [6]. More importantly, CP antennas are preferred for D2D application since they avoid any polarization mismatch problems in complex wireless channels [7]–[11].

Many investigations of OCP antennas in the microwave frequency range have been reported [12] – [24]. In general, two methods have been adopted to realize their OCP performance characteristics. One is to generate parallel electric and magnetic dipoles [12] – [21]; the other is to transform the linearly-polarized (LP) waves of a monopole into CP waves through a surrounding polarizer [22]. Unfortunately, none of these designs can be rescaled to mm-Wave frequencies such as the 28 GHz band simply because of the physical constraints associated with those much smaller wavelengths (e.g., 30 GHz has a 1.0 mm free space wavelength).

Only (to the best of our knowledge) two designs, [23] and [24], have been reported to date that realize OCP radiation characteristics in the mm-Wave band at 37 GHz and 38 GHz, respectively. The design in [23] consists of a LP omni-directional monopole radiator and a surrounding sleeve polarizer which transforms the radiated LP wave into a CP wave. However, its size is very large both electrically and physically, i.e., its electrical and physical diameters are, respectively, 4.7 λ_0 and 38 mm, λ_0 being the free-space wavelength at 37 GHz. The design in [24] has inclined slots etched on a circular waveguide to realize the OCP radiation. However, its volume: $\pi\ (7.435)^2 \times 25.05\ \text{mm}^3 = 2.84\ \lambda_0^2 \times 3.2\ \lambda_0 = 9.1\ \lambda_0^3$ at 38.3 GHz, is very large; and its fabrication is not cost-effective. Consequently, the previously reported two designs are not suitable for embedding into small portable devices such as smart phones, watches, and glasses.

In this paper, we introduce a compact 28 GHz OCP antenna for D2D applications in future 5G wireless networks. The overall size of the prototype disc-shaped antenna is compact, having the dimensions: $\pi\ (2.0)^2 \times 1.57\ \text{mm}^3 = 0.016\ \lambda_0^3$ at 28 GHz, which is more than a 200 times smaller transverse area than the reported 37 GHz system in [23] and 500 times smaller volume than the 38.3 GHz design in [24]. The paper is organized as follows. The OCP antenna design methodology and the optimized antenna configuration are described in Section II and Section III respectively. Section IV discusses the various effects associated with optimizing the key design parameters. The fabrication, assembly, and measurements of the 28 GHz OCP antenna prototype are described in Section V. Finally, conclusions are discussed in Section VI.

All simulation results reported in this paper were obtained with the ANSYS high frequency structure simulator (HFSS) version 17. The materials associated with these simulation models incorporated all of their known properties. Several prototypes were fabricated and tested. They all consistently reproduced the measured results reported herein.

II. Design Methodology

The design concept originated from the knowledge that different radiation patterns with diverse polarizations can be obtained by combining electric and magnetic dipoles with specific orientations and manipulating the phase difference between them. Two such variations are depicted in Fig. 2. If two orthogonally oriented electric and magnetic dipoles radiate in-phase with the same amplitude, Huygens source radiation, i.e, a uni-directional cardioid pattern, will be generated with the peak directivity being emitted broadside to the plane containing both dipoles. As shown in Fig. 2(a), the vertical loop current and the horizontal electric current lie in the yz plane but are oriented so that their dipole moments lie orthogonal to each other in the xy plane. The resulting pattern is cardioid-shaped and uni-directional along the z-axis. Many Huygens source antenna designs have been reported to date [25]–[35]. For instance, Luk and Wong first invented the LP magneto-electric (ME) dipole antennas based on this concept for base station applications [25], [26]. Electrically small Huygens dipole systems based on orthogonal electric and magnetic near-field resonant parasitic (NFRP) elements have been reported [32]–[35]. Recently, millimeter-wave CP versions of both the ME [28] and Huygens [29] dipole antennas have been reported for 5G applications.

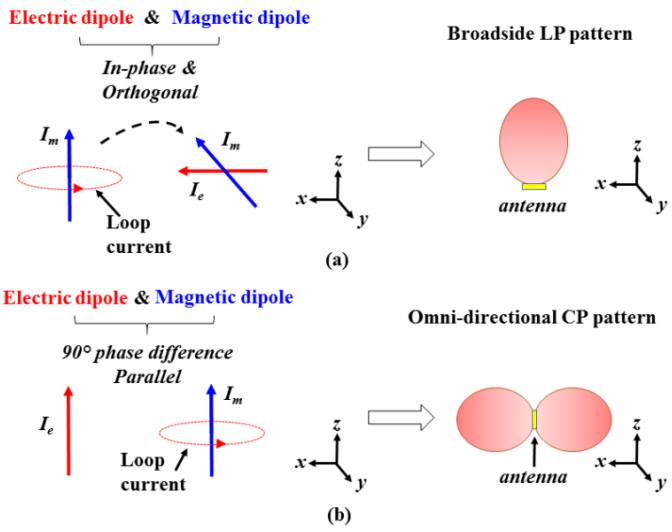

Fig. 2. Design concept of antennas formed with an electric and a magnetic dipole element. a) Huygens source. b) OCP antenna.

Our experience with these NFRP Huygens dipole antenna designs paved the way for the OCP antenna design illustrated in Fig. 2b. By rotating the electric dipole to be parallel to the magnetic dipole (as shown along the z-axis) and by exciting

them with a 90° phase difference, OCP radiation pattern will be generated [12]-[15], [17]-[24]. This should be contrasted with the ME or other Huygens dipole antenna systems for which the maximum directivity is along the direction orthogonal to the plane containing their orthogonal dipoles.

To further illustrate the OCP design concept, consider the electric dipole being oriented along the z-axis and the magnetic dipole being formed by a closed loop current in the xy-plane so its moment is also along the z-axis. The known far-field expressions for the resulting electric field components: E_θ for a small electric dipole and E_φ for a small magnetic dipole are [36]:

$$E_\theta = jk\ \eta\,[I_e L]\cdot\frac{e^{-jkr}}{4\,\pi\,r}\cdot\sin\theta \quad \textit{Small Electric Dipole} \quad (1)$$

$$E_\varphi = jk\,[I_m L]\cdot\frac{e^{-jkr}}{4\,\pi\,r}\cdot\sin\theta \quad \textit{Small Magnetic Dipole} \quad (2)$$

where $k = 2\pi/\lambda$ is the wave number; I_e is the magnitude of the electric dipole; I_m is the magnitude of the electric dipole; L is the length of the electric dipole; $I_e L$ is the electric dipole current moment; $I_m L$ is the magnetic dipole current moment; and η is the wave impedance. One can see immediately that if $j\,\eta\,I_e = I_m$, then omni-directional CP radiation will be generated. Moreover, it is also known that a current loop of area A in free-space, which is driven with a constant current I_0, yields $I_m = j\,A\,\omega\mu_0\,I_0/L$ [36]. From this, one finds that if a current loop can be generated in the plane orthogonal to the dipole, then its magnetic dipole moment will have the correct orientation. Furthermore, it will naturally have the correct 90° phase relative to the electric one. Consequently, the OCP design target is to realize a vertical electric current (electric dipole) along with a surrounding loop current (magnetic dipole) in such a manner that they have the appropriate amplitudes and phases in a compact configuration at 28GHz.

III. Antenna Design

The OCP target design evolved from a variety of NFRP antenna experiences. Its operating principles were clarified with HFSS parameter studies. They also led to the final, optimized version.

A. Antenna configuration

The OCP antenna configuration is shown in Fig. 3. As noted, the Rogers™ 5880 copper-cladded substrate was used for this design. Its relative permittivity and permeability are, respectively, 2.2 and 1.0; its loss tangent is 0.0009. Traces are printed on the upper and bottom surfaces of a single disc-shaped piece of the substrate. These top and bottom traces are 17 μm thick (0.5 oz) copper; they are connected through the substrate by copper-plated via holes. The entire structure is excited by a coax feed line. A common vertical monopole radiator is located in the center and is attached directly to the center conductor of the coax. The monopole goes vertically through the substrate and is terminated with a conducting disc that lies on its top surface. Four thin straight radial lines separated by 90° extend from this center conductor to the outside edge of the substrate. The end of each line joins a 27° arc-loop trace whose outside edge coincides with the edge of the substrate. These four meandered branches act as top-hat loading of the monopole. The end of each arc-loop is connected to a vertical, plated via hole, which in turn is connected to a 52° arc-loop printed on the bottom face of the substrate disc. All of the top and bottom arc-loop traces have the same width, W_{arc}. The radial traces and the top and bottom arc-loops thus form a wheel-shaped structure. The inner circle of a ground plane annular disk is connected directly to the outer surface of the coax. The outer edge of this grounded disc is separated by a distance W_{gap} from inner edges of the bottom arc-loop traces.

The via structures are straightforward to fabricate with standard PCB manufacturing technologies. The entire disc-shaped OCP structure is simple, easy to manufacture, and is very compact, its overall size being only: $\pi\,(1.72)^2 \times 1.0\ \text{mm}^3 = 0.081\ \lambda_0^2 \times 0.09\ \lambda_0 = 0.0076\ \lambda_0^3$ at 28 GHz. Thus, it could easily fit into many anticipated small 5G wireless devices. Moreover, as only one piece of dielectric substrate is needed, this design is cost-effective and mass production is possible. The detailed and optimized antenna parameters of the simulated OCP antenna are listed in Table I.

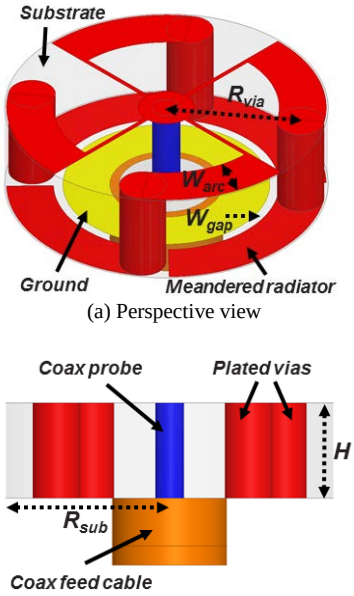

(a) Perspective view

(b) Side view

Fig. 3. OCP antenna configuration. (a) Perspective view. (b) Side view.

TABLE I
OCP Antenna Design Parameters

Parameter	Description	Value
R_{sub}	Radius of the substrate (antenna)	1.72 mm
R_{via}	Radius to the center of the plated vias	1.45 mm
D_{via}	Diameter of the plated vias	0.5 mm
D_{probe}	Diameter of the center vertical radiator	0.3 mm
D_{coax}	Diameter of the coaxial cable	1.2 mm
W_{arc}	Width of the arc-loop stubs	0.5 mm
L_{arc}	Length of each arc-loop stub	3.41 mm
A_{upper}	Angle swept by the upper arc-loop stub	56 deg
A_{bottom}	Angle swept by the bottom arc-loop stub	79 deg
W_{gap}	Gap between ground and loop stubs	0.1 mm

H	Thickness of the substrate	1.0 mm
L_{coax}	Length of the coaxial feeding line	0.5 mm

B. *Operating principles*

Fig. 4 depicts the currents flowing on the metal components of the OCP structure. As indicated, the currents on the top and bottom arc-loops and the ground plane disc complete the current loop that creates the magnetic dipole and, hence, the primary contributions to the E_φ components in the far-field. Similarly, while the vertical currents on the monopole and on those on the four vias are in phase, those on the monopole dominate their combined effects. This collective behavior creates the electric dipole and, hence, the primary contributions to the E_θ components in the far-field. Consequently, the electric and magnetic dipoles are oriented parallel to each other.

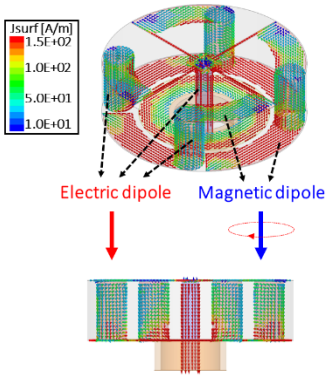

Fig. 4. Current distributions on the OCP antenna structure at 28GHz. The corresponding electric and magnetic dipole moments and the effective are depicted.

Note in Fig. 4 that the currents in the monopole and the vias are all pointing downwards and, hence, the electric dipole also points in the –z-direction. Furthermore, the loop currents are clockwise along the top and bottom arc-loops as depicted. As a result, the magnetic dipole is also pointing downward, in the same direction as the electric dipole. These behaviors confirm the parallel orientation of the electric and magnetic dipoles. It is noted that the total length of the monopole, radial arm, arc-loop, via, and arc-loop is 0.508 λ_0. Hence, the actual electric length is $\ell_e = 0.508\,\lambda_0 \cdot \sqrt{\varepsilon_r} \approx 0.75\lambda_0$ for the substrate whose ε_r = 2.2. Consequently, the current distribution on each radiating branch acts like a $\frac{3}{4}\lambda_0$ monopole or equivalently, a 1.5 λ_0 dipole. Similarly, the electrical circumferance of the loop $\ell_m = 2\pi\, R_{sub} \cdot \sqrt{\varepsilon_r} \approx 1.497\lambda_0$. Thus, the electric and magnetic dipoles are self-resonant and their phases yield their co-directional orientations, as illustrated in Fig. 4.

To illustrate the phase difference between these dipoles, Fig. 5 shows plots of the currents on the OCP structure at four different quarter-periods when it is driven at 28 GHz. The vertical and loop currents are changing simultaneously; one observes that their max and min values are in-phase. On the other hand, from the E-field expressions associated with the dipole and loop current one would expect that their far-field behavior would naturally exhibit a 90° phase difference. To quantify the actual phase difference, the magnitudes and phases of the two electric field components, E_θ and E_φ, at 28 GHz in the far-field are plotted in Fig. 6. One finds that their magnitudes are nearly the same as required for circular polarization. On the other hand, one finds that their phase difference is around 72° and that this value is stable across a wide range of elevation angles. The realized 72° phase difference is less than the ideal 90° because there is a slight phase difference between the center vertical and the surrounding arc-loop currents. Furthermore, because the sign of the difference between the phase values of E_θ and E_φ is negative, one finds that the OCP configuration in Fig. 3 generates RHCP radiation.

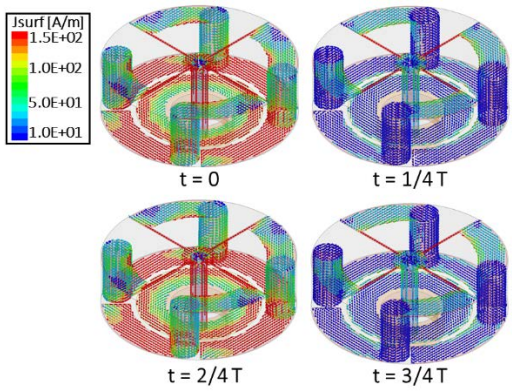

Fig. 5. Current distributions on the OCP antenna structure at 28GHz for the first four quarter periods.

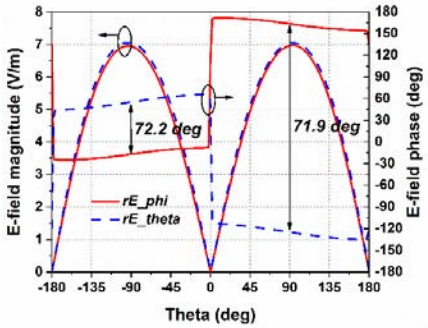

Fig. 6. Simulated magnitudes and phases in the vertical plane: φ = 0°, of the two orthogonal electric field components, E_q and E_φ, generated in the far field of the OCP antenna.

As the two key conditions for realizing CP radiation: nearly equal magnitude and nearly 90° phase difference, were achieved, the simulated OCP radiation characteristics were explored. Fig. 7(a) gives the reflection coefficient and axial ratio (AR) results as functions of the source frequency, as well as the far-field patterns at 28 GHz. The simulated -10-dB impedance bandwidth is 1.5 GHz, from 27.0 to 28.5 GHz; the 3-dB axial ratio (AR) bandwidth is 3.1 GHz, from 25.5 to 28.5 GHz. The shaded region denotes the overlap between these two bandwidths. It extends from 27 to 28.5 GHz, which covers the entire 27.5 to 28.35 GHz band dedicated for 5G wireless applications. As Fig. 7(b) illustrates, very good omni-directional CP radiation patterns are produced at 28 GHz with the peak RHCP realized gain being 2.0 dBic. The gain

difference around the entire horizontal plane (θ = 90°) is less than 0.1 dB. Moreover, similar radiation performance is obtained throughout the entire 5G 28 GHz band.

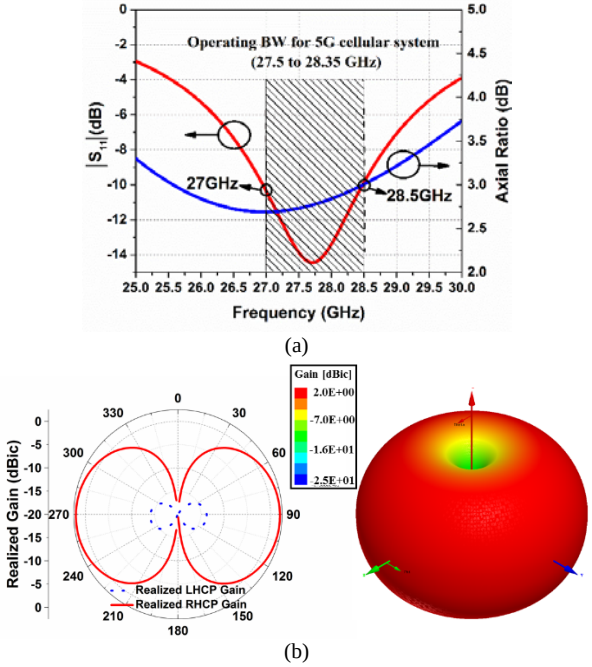

Fig. 7. Simulated OCP antenna performance characteristics. a) $|S_{11}|$ and axial ratio values (φ = 0°, θ = 90°) as functions of the source frequency. b) 2D RHCP and LHCP realized gain patterns in the vertical plane φ = 0° at 28 GHz and the corresponding 3D realized gain pattern at 28 GHz.

IV. Study of the Key Design Parameters

The OCP antenna performance was optimized by identifying the key design parameters. In particular, the height and radius of the OCP antenna, the length and width of the arc-loop pieces, and the number of meandered radiators (i.e., the number of arc-via-based elements) were found to be critical. Moreover, it was established that the actual orientations of the arc-loop pieces determine whether the CP radiation is right or left handed. Furthermore, as will be demonstrated, an electrically-small OCP structure can be obtained simply by loading the design with a dielectric substrate having a higher permittivity value.

(a) Height and radius of the OCP antenna

The dimensions of the OCP antenna: the radius R_{via} and the height H, primarily determine the impedance matching AR bandwidth. First, the height of the OCP antenna noticeably affects the E_θ component that arises from the central, vertical radiator. This behavior is observed readily by considering the radiation resistance, R_a, of the OCP antenna as shown in Fig. 8(a). Simulations indicate that R_a is 19, 31, and 73 ohms at the resonance frequency when the antenna height is 0.8, 1.0, and 1.2 mm, respectively. This R_a outcome confirms that the radiation resistance increases as the length of the central vertical radiator increases, i.e., as the electric dipole strength increases. Fig. 8(b) presents a comparison of the $|S_{11}|$ and the AR values as functions of the source frequency when the antenna height is 0.8, 1.0, and 1.2 mm, respectively. It is recognized quickly that the impedance matching is poor when the height is 0.8 mm, i.e., R_a is too small to achieve good impedance matching. On the other hand, although the matching is much better when the height is 1.2 mm, the AR values quickly increase resulting in a poor overlap of the 3-dB AR frequency band with the impedance matched frequency band. Consequently, the 1.0 mm height was selected for the final design.

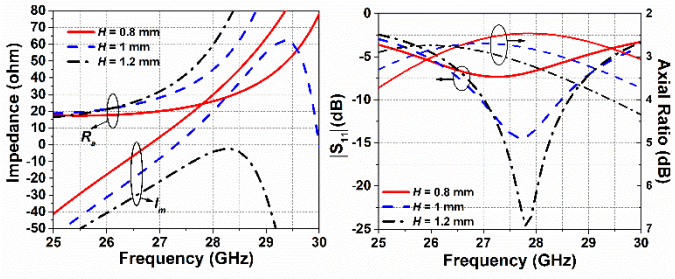

Fig. 8. Simulated performance characteristics of the OCP antenna as functions of the source frequency when the antenna height H is 0.8, 1.0, and 1.2 mm. a) Real and imaginary parts of the OCP antenna input impedance. b) $|S_{11}|$ and AR values (φ = 0°, θ = 90°).

With the width of the arc-loop stubs, W_{arc}, fixed, the radius R_{via} controls the overall radius of the OCP antenna, which is the dominant design parameter that determines its operational center frequency, f_c. Fig. 9(a) clearly demonstrates this point. Both the impedance and AR bandwidths move to a higher range of frequencies when R_{via} changes from 1.55 to 1.35 mm in steps of 0.1 mm. Similarly, with R_{via} fixed, W_{arc} then controls the antenna's radius. Fig. 9(b) confirms that as W_{arc} is varied from 0.6 to 0.4 mm in steps of 0.1 mm, the same behavior occurs. However, one finds by comparing Figs. 9(a) and 9(b) that R_{via} is a coarse-tuning parameter and W_{arc} is a fine-tuning one. The choices R_{via} = 1.45 mm and W_{arc} = 0.5 mm were made so that the design covers the 5G 28 GHz band, from 27.5 to 28.35 GHz.

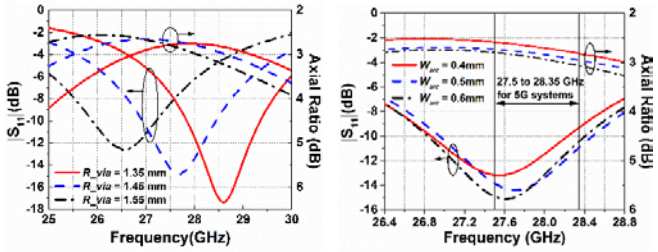

Fig. 9. Simulated $|S_{11}|$ and AR values (φ = 0°, θ = 90°) of the OCP antenna as functions of the source frequency. a) When the antenna radius R_{via} is 1.35, 1.45, and 1.55 mm. b) When the width of the arc-loops, W_{arc}, is 0.4, 0.5, and 0.6 mm.

(b) Width and length of the arc-loop elements

Analogous to the impact that the height of the OCP antenna has on the electric dipole strength, the width, W_{arc}, of the arc-loop elements also affects the magnetic dipole strength and, hence, the AR values. In particular, the magnitude of E_φ will

increase if W_{arc} increases. Fig. 9(b) confirms this behavior. The AR values increase as W_{arc} increases, while the impedance matching improves. Thus, the width W_{arc} = 0.5 mm was also selected to obtain the desired overlapping impedance matching and -3-dB AR bandwidths that cover the 5G 28 GHz band.

Due to the resonant nature of the OCP antenna, the length of the arc-loop radiators (indicated by the angles swept out by those arcs, A_{upper} and A_{bottom}) impacts both the impedance and AR bandwidths. Varying the angle A_{upper} (A_{bottom}) changes the length of the arc-loop radiator on the upper (bottom) layer of the OCP antenna. One parameters study, summarized in Fig. 10(a), studied the effect of varying A_{upper} from 53° to 59° in steps of 3º with A_{bottom} held fixed. As shown, both the $|S_{11}|$ and AR values move to a lower frequency range as A_{upper} increases. A second study, whose results are shown in Fig. 10(b), demonstrates that the resonance frequency and the AR bandwidth also move to a higher frequency range as A_{bottom} decreases from 79° to 77° in steps of 1° with A_{upper} held fixed. It is further noted that the impedance matching is less sensitive to variations in A_{upper} than it is to those in A_{bottom}. This behavior occurs, as shown in Fig. 4, because the current distributions on the bottom arc-loops are much stronger than they are on the upper arc-loops.

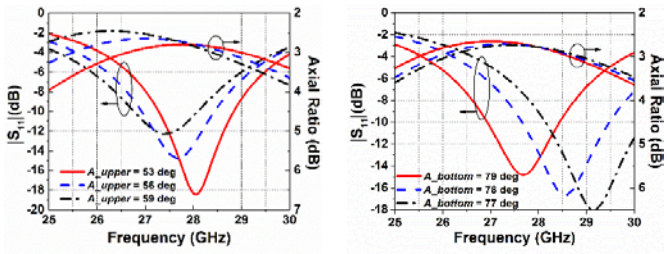

(a) (b)

Fig. 10. Simulated $|S_{11}|$ and AR values (φ = 0°, θ = 90°) of the OCP antenna as functions of the source frequency. a) When *A_upper* is 53º, 56º, and 59º. b) When *A_bottom* is 79º, 78º, and 77º.

(c) Number of the meandered radiators

It was determined that there is an optimum number of arc-loop elements ("branches") to achieve the desired overlapping impedance and AR bandwidths, as well as omni-directional patterns with very tiny ripples. Three models were considered by adjusting the parameters R_{via}, A_{upper} and A_{bottom}. Referring to Fig. 11, the designs were: Three Branches: A_{upper} = 53°, A_{bottom} = 97°, R_{via} = 1.45 mm; Four Branches: A_{upper} = 56°, A_{bottom} = 97°, R_{via} = 1.45 mm; and Five Branches: A_{upper} = 54°, A_{bottom} = 60°, R_{via} = 1.7 mm. Fig. 11(a) shows that all the models realize an impedance bandwidth that covers the 5G 28 GHz band. Similarly, Fig. 11(b) shows that all of the models produce the same co-polarization realized gain values. However, it also clearly shows that the three-branch model has large ripples in its cross polarization due to its less symmetrical structure in the azimuth plane. On the other hand, while its ripples are much smaller and similar to the four-branch values, the five-branch model exhibits much larger cross-pol values. Note that the largest discrepancy in the cross polarization occurs between the vertical planes φ = 90° and φ = 270° for the three-branch case. The magnitude and phase of the orthogonal components of the electric field, E_φ and E_θ, in the vertical plane φ = 90° are given for the three-branch model in Fig.12(a). It is clearly seen that the maximum phase difference variation between E_φ and E_θ in the θ = 90° and the θ = -90° directions is 6.2°. This difference is much larger than obtained with the four-branch model, 0.3°. Moreover, the magnitudes of both E_φ and E_θ are different because the strength of the magnetic dipole becomes smaller with fewer branches. Consequently, the three-branch model also exhibits poor omni-directivity.

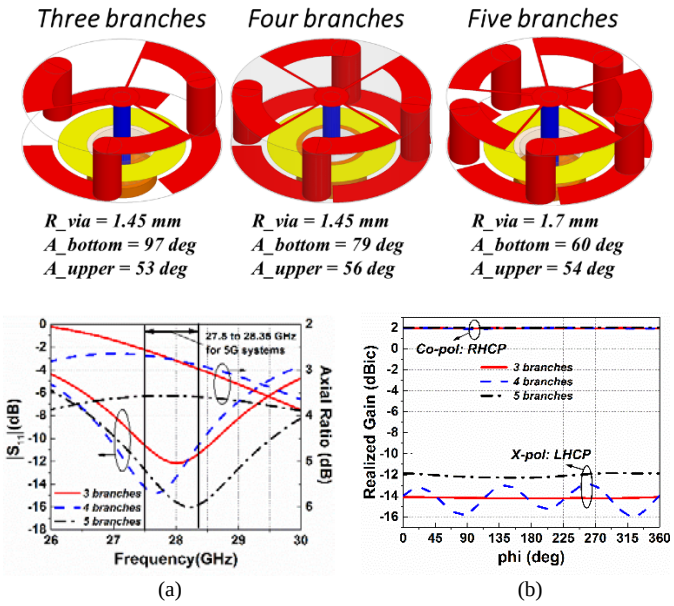

(a) (b)

Fig. 11. Simulated performance characteristics of the OCP antenna with three, four and five branches. a) $|S_{11}|$ and AR values (φ = 0°, θ = 90°) as functions of the source frequency. b) Radiation patterns in the azimuth plane (θ = 90°) at 28 GHz.

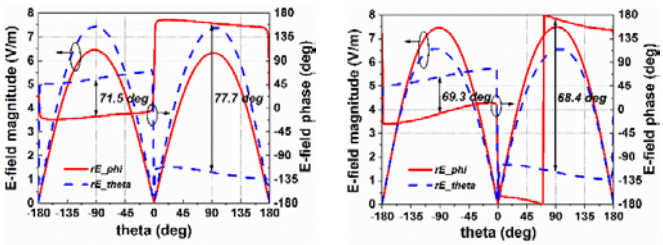

(a) (b)

Fig. 12. Simulated magnitudes and phases in the vertical plane: φ = 0°, of the two orthogonal electric field components, E_q and E_φ, generated in the far field of the OCP antenna. a) OCP antenna with three branches. b) OCP antenna with five branches.

On the other hand, both the four- and five-branch models produce good omni-directional patterns with very tiny ripples. Fig. 12(b) shows that the phase difference variation for the five-branch model is only 0.9º between the θ = -90° and θ = 90° directions at φ = 0° plane. Moreover, as more branches are introduced, the strength of the magnetic dipole becomes larger. This negatively impacts the AR values as shown in Fig. 11(a). Furthermore, as shown in Fig. 12(b), the phase difference between E_φ and E_θ that occurs in the five-branch model

becomes smaller, i.e., it is 69.3°. This means that it is further away from the ideal 90°. As the result, the corresponding AR values across the entire 5G 28 GHz band are larger than 3 dB. These case studies confirm that the four-branch OCP antenna is the optimal design.

(d) Sense of Rotation of the arc-loop elements

The circular polarization type, RHCP or LHCP, was found to be dependent on the orientation of the arc-loop elements since the currents impressed on them define the direction of the magnetic dipole. The two possible orientations and the resulting currents impressed on the OCP structure are illustrated in Fig.13. If the four branches are oriented in a clockwise rotation sense, the electric and magnetic dipoles point in the same –z-direction. As a consequence, the relative phase of E_φ is behind that of E_θ and RHCP radiation results. On the other hand, if the four branches rotate in an anti-clockwise manner as they do in the optimized design, the electric and magnetic dipoles will point in opposite directions along the z-axis. The relative phase of E_φ is then ahead of E_θ and LHCP radiation results. It is noted that a polarization reconfigurable OCP antenna is thus feasible simply by introducing RF switches on the arc-loop elements.

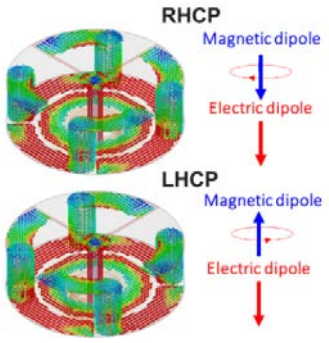

Fig. 13. Loop stub orientations for RHCP/LHCP radiation.

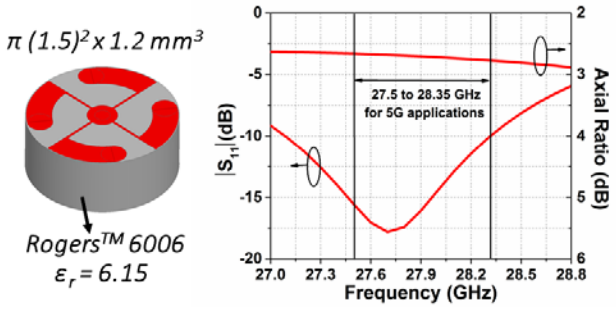

Fig. 14. Electrically-small OCP antenna (ka = 0.95) and its performance characteristics achieved by using instead the Rogers™ 6006 substrate, which has a higher relative permittivity: ε_r = 6.15.

(e) Impact of a Higher Permittivity Substrate

It was found that the OCP antenna can be reduced in size simply by introducing a substrate with a higher permittivity value and retuning the design parameters. In fact, one can realize an electrically-small version in this manner. By replacing the Rogers™ 5880 substrate with the Rogers™ 6006 substrate having ε_r = 6.15, and by setting R_{sub} = 1.5 mm, H = 1.2 mm, A_{upper} = 56°, and A_{bottom} = 65°, the electrical size is reduced from ka = 1.02 to ka = 0.95, where $k = 2\pi/\lambda$ and a is the radius of the smallest sphere enclosing the antenna. The simulated performance characteristics of this electrically-small design are displayed in Fig. 14. Again, its OCP bandwidth covers the entire 28 GHz 5G applications band.

V. Measured Prototype

To verify the OCP antenna design concepts, a prototype was fabricated, assembled, and tested. Standard and low-cost printed circuit board (PCB) processes were used to fabricate the OCP components. As will be discussed, there were some measurement challenges, such as leakage currents and accurate alignment, because the antenna under test (AUT) was very tiny and compact. Nevertheless, the measured results are in good agreement with their simulated values.

A. Fabricated OCP antenna prototype

Because the physical size of the OCP antenna is tiny, the effects of the leakage currents from the comparatively long coax feedline are not negligible. At 28 GHz, the diameter of the coax cable, 1.2 mm, is large in comparison to the antenna structure. Sleeve baluns had to be incorporated into the feedline for the actual measurements. The baluns choke off any leakage currents that may occur on the outer surface of the measurement cables. In the final prototype, two baluns were added on the cable to eliminate the unwanted radiation from the outer surface of the coax feedline. One is located below the OCP antenna with a gap of 1 mm. Another is 10 mm away above the K-connector. At the same time, the antenna structure had to be adjusted slightly to accommodate the presence of the baluns. Moreover, for convenience and for simplicity of fabrication and assembly, we elected to use the commercially available Rogers™ 5880 substrate with the standard thickness of 1.575 mm. The antenna was fabricated by Chengdu Tomorrow High Technology Co., Ltd. with standard PCB manufacturing technologies. The sleeve baluns were manufactured from copper. Their lengths were 1.8 mm and they had a wall thickness of 0.5 mm. The feedline was the 047 Semi-rigid coax cable with copper inner and outer conductors. The maximum operating frequency of this cable is 40 GHz. A K-connector was soldered to the end of the cable; it also works also up to 40 GHz. Both the cable and the connector are manufactured by Pasternack Enterprises, Inc.

The prototype design parameters are listed in Table II. The final dimensions of the fabricated antenna prototype were: $\pi\,(2.0)^2 \times 1.57$ mm^3 = 0.016 λ_0^3 at 28 GHz. Figure 15 presents a photo of the fabricated OCP antenna prototype and enlarged microscope images of it.

TABLE II
PARAMETERS OF OCP ANTENNA PROTOTYPE WITH LONG COAX AND BALUN

Parameter	Description	Value
R_{sub}	Radius of the substrate (antenna)	2.0 mm
R_{via}	Radius to the center of the plated vias	1.45 mm

D_{via}	Diameter of the plated vias	0.5 mm
D_{probe}	Diameter of the center vertical radiator	0.3 mm
D_{coax}	Diameter of the coaxial cable	1.2 mm
W_{arc}	Width of the arc-loop stubs	0.5 mm
L_{arc}	Length of each arc-loop stub	3.26 mm
A_{upper}	Angle swept by the upper arc-loop stub	56 deg
A_{bottom}	Angle swept by the bottom arched stub	73 deg
W_{gap}	Gap between ground and loop stubs	0.1 mm
H	Thickness of the substrate	1.575 mm
L_{coax}	Length of the coaxial feeding line	15.0 mm

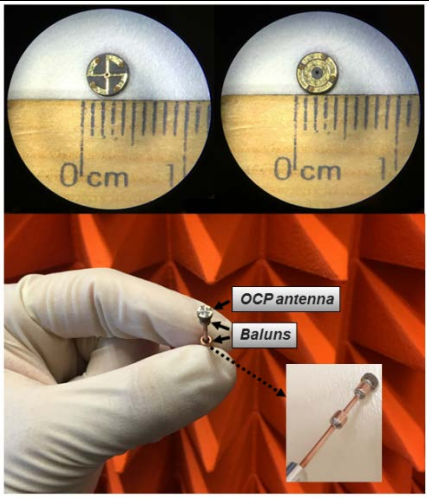

Fig. 15. Photos of the fabricated OCP antenna prototype with enlarged microscope images (left: top view; right: bottom view).

B. *Measurement setup*

The 28GHz OCP antenna prototype was measured in the anechoic chamber at the Royal Melbourne Institute of Technology (RMIT). A schematic of the far-field measurement used is shown in Fig. 16(a). A calibrated standard dual-ridged ETS-Lindgren horn antenna (Type: ETS 3116 operating from 18 to 40 GHz) was used as the source antenna. The OCP prototype was measured as the receiving antenna. A SHF-810 transmit medium power amplifier and a Miteq JS4-1800-4000-40-5A (18−40 GHz) receiver amplifier were employed to ensure that the received power level from the transmitting antenna to the AUT was high enough to provide stable power reception. The data from the dual-linear polarized horn antenna was recorded and used to calculate the CP radiation performance of the OCP antenna. The OCP AUT anechoic chamber setup is illustrated in Fig. 16(b).

C. *Measured results*

The $|S_{11}|$ values were measured with an Anritsu VectorStar MS4644B Vector Network Analyzer (VNA). A comparison of the measured and simulated results is given in Fig. 17(a). The measured resonance frequency, 27.8 GHz, agrees well with its 28 GHz simulated value. The measured -10-dB impedance bandwidth is 2.2 GHz, from 26.4 to 28.6 GHz, which is a bit wider than its simulated value, 1.7 GHz. This difference is most likely due to cable losses and fabrication tolerances. The measured and simulated realized RHCP gain values are shown in Fig. 17 (a). They are also in good agreement.

The measured and simulated AR values are compared in Fig. 17(b). The measured 3-dB AR bandwidth is 2.65 GHz, from 26.5 to 29.15 GHz. The overlap of the -10-dB impedance and the 3-dB-AR bandwidths extends from 26.5 to 28.7 GHz, yielding a 2.2 GHz bandwidth. This band of frequencies covers the entire proposed 27.5 to 28.35 GHz band for 5G wireless systems. The measured and simulated AR values agree very well. The measured AR values above 29.15 GHz, outside of the 28 GHz band, become a little bit larger than their simulated counterparts. This outcome is most likely due to AUT alignment issues. It proved to be quite difficult to achieve good alignment (for both concentricity and elevation) because of the tiny size and high operating frequency of the OCP prototype.

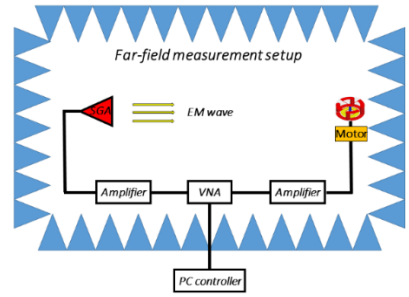

(a)

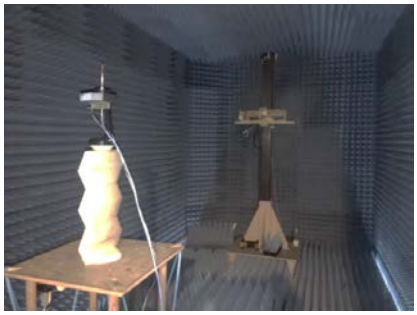

(b)

Fig. 16. The OCP antenna measurement setup. a) Block diagram. b) Photo of the actual measurement environment.

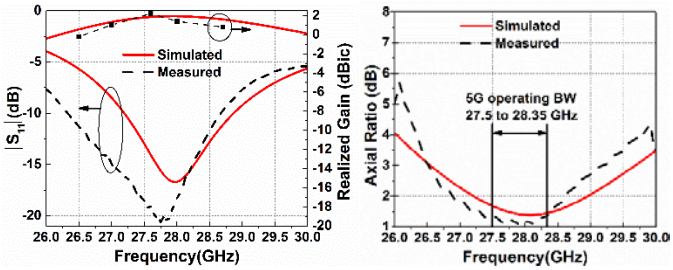

(a) (b)

Fig. 17. Simulated and measured (a) $|S_{11}|$ and realized gain values, and the (b) AR values of the OCP antenna (φ = 0°, θ = 90°).

The measured and simulated normalized realized gain patterns in the two vertical planes, φ = 0° and φ = 90°, are given in Fig. 18. They are plotted at 26.5, 27.6, and 28.7 GHz, i.e., at the center frequency and at the two edge frequencies of the measured operational bandwidth. The normalization values are the peak realized gain values at each frequency: -0.2 dBic at 26.5 GHz, 2.2 dBic at 27.6 GHz, and 0.8 dBic at 28.7 GHz.

These measured and simulated results are also found to be in reasonable agreement. Clearly, the predicted OCP radiation patterns were realized. The measured (simulated) maximum realized RHCP gain was 2.2 (2.0) dBic. The simulated radiation efficiency is high, > 95%, across the entire operating bandwidth. The slight difference in the maximum measured realized gain from its simulated value is again attributed to measurement alignment and fabrication tolerances.

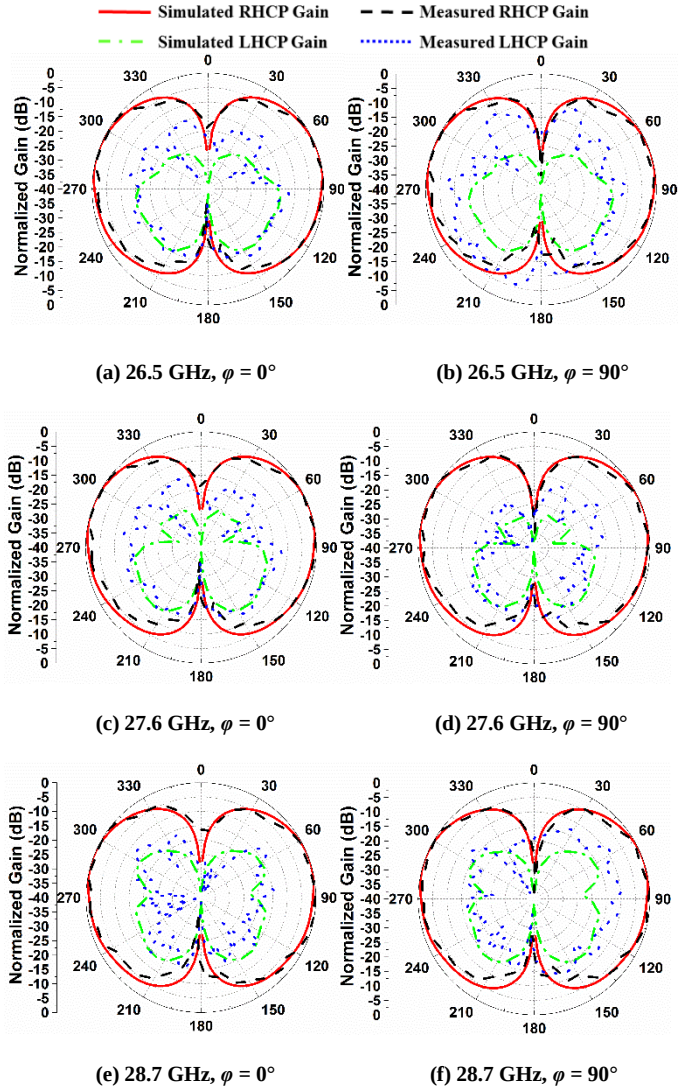

Fig. 18. Simulated and measured normalized realized gain patterns of the OCP antenna at its center frequency, 27.6 GHz, and at the two edge frequencies of its measured operational bandwidth, 26.5 GHz and 28.7 GHz in the two vertical planes: Left: φ = 0° plane; Right: φ = 90°.

The omni-directional radiation characteristics of the prototype OCP antenna were evaluated and the results are presented in Fig. 19 at the same frequencies. The measured and simulated normalized realized gain patterns and AR values are plotted in the horizontal (θ = 90º) plane. One observes that good omni-directional CP patterns were realized. The maximum measured variation in the co-pol RHCP realized gain pattern is only 0.7 dB at the center frequency, 27.6 GHz. While it is 0.1 dB in simulations, this measured outcome is quite reasonable. In addition, Fig. 19 also shows that the average AR values at all three frequencies are less than 3 dB. Again, the differences between the measured and simulated AR values are quite reasonable and are attributed primarily to the measurement alignment issues. These small measured gain variations in the omni-directional patterns provide further confirmation of the effectiveness of the four-branch design.

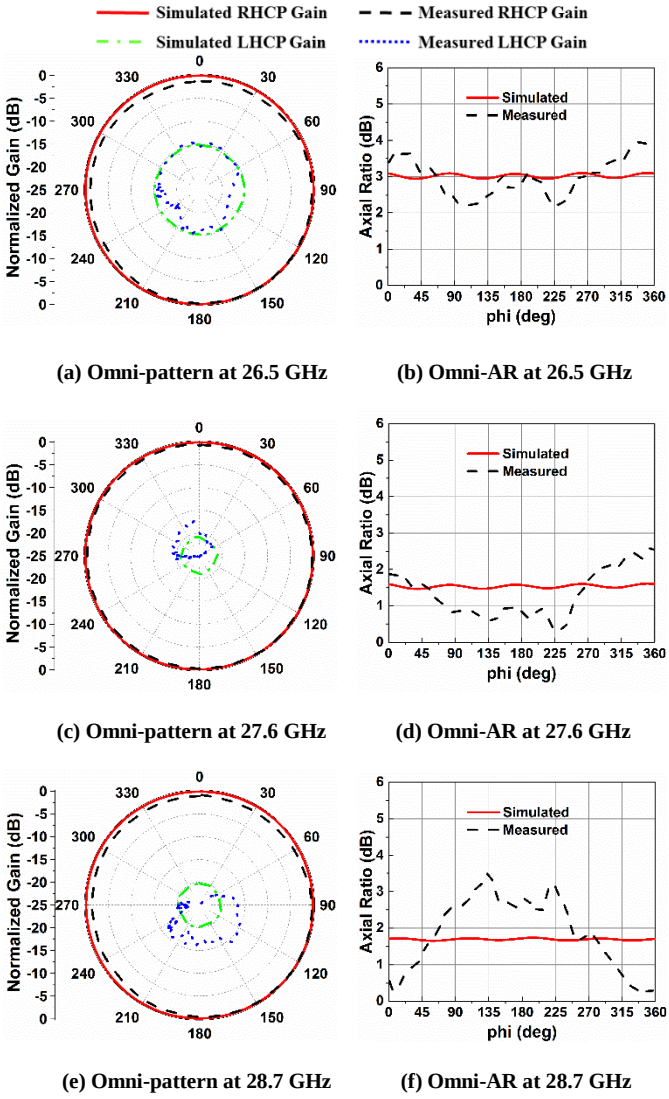

Fig. 19. Simulated and measured omni-directional normalized realized gain patterns in the horizontal plane (θ = 90º) and the corresponding AR values of the OCP antenna at its center frequency, 27.6 GHz, and at the two edge frequencies of its operating bandwidth, 26.5 GHz and 28.7 GHz.

These measured results verified our OCP design concept. A simple and compact 28 GHz OCP antenna was successfully realized. Table III compares the dimensions, operating frequency, bandwidth, axial ratio value, gain, radiation efficiency and number of parts required to assemble the antenna (which reflects the fabrication complexity), for all of the referenced OCP antennas in [12] – [15], [17] – [24] and our realized prototype. This comparison clearly verifies that our design has outstanding characteristics, especially when taking into account its electrical size. Moreover, it has many attractive practical features that would be desirable for applications in the Ka band. These include a simple fabrication process and an

easy to assemble, compact design. Moreover, our OCP antenna is unique simply because it is the only one currently available for future D2D applications in the 5G 28 GHz band.

TABLE III
DESIGN COMPARISONS OF THE OCP ANTENNAS REPORTED IN THE LITERATURE TO DATE

Ref.	f_c (GHz)	Dimensions (in λ_0)	ka	Usable CP FBW (%)	AR (f_c) (dB)	Type, Peak Gain (dBic)	RE (f_c) (%)	Number of parts for assembly	Fabrication Complexity
[12]	1.575	rad = 0.26; h = 0.08	1.65	11.40%	1.91	RHCP, 1.51	NA	2 PCBs + 6 pins	Medium
[13]	2.44	0.22 × 0.22 × 0.076	1.01	3.56%	1.88	LHCP, 1.39	NA	1 PCB + 4 copper rods	Medium
[14]	2.42	rad = 0.20, h = 0.18	1.38	5.3%	~1.2	LHCP, 1.12	76	1 PCB	Simple
[15]	0.915	0.32 × 0.32 × 0.52	2.17	2.2%	~2.0	RHCP, 2.00	95	2 PCBs	Medium
[17]	2.0	rad = 0.19; h = 1.56	5.04	41%	~2.8	LHCP, 2.50	NA	2 PCBs + 2 copper rods	Medium
[18]	2.44	rad = 0.73, h = 0.02	4.59	18.40%	~1.0	RHCP, 4.00	90	1 PCB	Simple
[19]	3.4	0.34 × 0.34 × 0.28	1.75	22%	~2.2	LHCP, 1.0	90	1 DRA + 1 monopole	Simple
[20]	5.75	1.72 × 0.31 × 0.04	5.49	4.35%	1.3	LHCP, 2.4	48	1 PCB	Simple
[21]	2.4	0.5 × 0.2 × 0.06	1.70	NA	2.6	RHCP, 0.0	NA	9 PCBs + 1 metallic wall	Complex
[22]	5.3	rad = 0.58; h = 0.55	4.03	41.00%	1.3	LHCP, 3.5	NA	8 dielectric slabs + 1 monopole	Complex
[23]	**36.85**	**rad = 2.34; h = 0.86**	**14.9**	**0.80%**	**2.8**	**RHCP, 3.2**	**NA**	**1 polarizer + 1 monopole**	**Medium**
[24]	**38.3**	**rad = 2.5; h = 5.1**	**22.4**	**1.80%**	**1.1**	**LHCP, 1.5**	**NA**	**Waveguide + Polarizer + Short**	**Complex**
This work	**28**	**rad = 0.19; h = 0.15**	**1.28**	**8.0%**	**1.2**	**RHCP, 2.2**	**95**	**1 PCB**	**Simple**

VI. CONCLUSIONS

An antenna design was presented that achieved omni-directional CP radiation performance in a simple, compact structure operating at 28GHz. The design methodology was explained. Effective, parallel-oriented electric and magnetic dipoles were developed that produced approximately the same far-field magnitudes of the orthogonal, transverse to the direction of power propagation, electric field components with the appropriate phase difference to realize OCP radiation performance with either RHCP or LHCP characteristics. The impact that several key design parameters had on the OCP antenna's performance characteristics were discussed. The fabrication, assembly, and testing of an OCP antenna prototype were described. It was demonstrated that the experimental results verified the design concepts and were in good agreement with their simulated values. A comparison of the prototype OCP antenna to other designs reported in the literature demonstrated, to the best of our knowledge, that our OCP antenna is the first realized at 28 GHz that has a simple and compact structure, is easy to fabricate, and completely covers the proposed 5G 28 GHz applications band. This OCP antenna is a good candidate for 5G wireless systems, specifically for D2D communication applications.

VII. ACKNOWLEDGEMENTS

The authors would like to thank Prof. Y. Jay Guo, University of Technology Sydney, for his support of these efforts; Dr. Hang Wong from City University of Hong Kong and Prof. Ming-Chun Tang from Chongqing University for their fabrication guidance in the measurement campaign; and finally, RMIT for hosting our measurement efforts.

REFERENCES

[1] T. S. Rappaport, S. Sun, and R. Mayzus, "Millimeter wave mobile communications for 5G cellular: It will work!" *IEEE Access*, vol. 1, pp. 335–349, 2013.

[2] "Fact Sheet: Spectrum Frontiers Order To Identify, Open Up Vast Amounts Of New High-Band Spectrum For Next Generation (5G) Wireless Broadband", Federal Communications Commission, Washington, DC, USA, July. 2016. [Online]. Available: https://apps.fcc.gov/edocs_public/attachmatch/DOC-340310A1.pdf.

[3] M. N. Tehrani, M. Uysal and H. Yanikomeroglu, "Device-to-Device communication in 5G cellular networks: Challenges, solutions, and future directions," *IEEE Commun. Mag*., vol. 52, no. 5, pp. 86-92, Feb. 2014.

[4] W. Roh, J.-Y. Seol, J.-H. Park, B. Lee, J. Lee, Y. Kim, J. Cho, and K. Cheun, "Millimeter-wave beamforming as an enabling technology for 5G cellular communications: theoretical feasibility and prototype results," *IEEE Commun. Mag.*, vol. 52, no. 2, pp. 106-113, Feb. 2014.

[5] W. Hong, K. H. Baek, Y. Lee, Y. Kim and S. T. Ko, "Study and prototyping of practically large-scale mmWave antenna systems for 5G cellular devices," *IEEE Commun. Mag.*, vol. 52, no. 9, pp. 63-69, Sep. 2014.

[6] T. S. Rappaport, G. R. MacCartney, M. K. Samimi and S. Sun, "Wideband millimeter-wave propagation measurements and channel models for future wireless communication system design," *IEEE Trans. Commun.*, vol. 63, no. 9, pp. 3029-3056, Sep. 2015

[7] N. Nguyen-Trong, L. Hall, and C. Fumeaux, "A frequency- and polarization-reconfigurable stub-loaded microstrip patch antenna," *IEEE Trans. Antennas Propag.*, vol. 63, no. 11, pp. 5235–5240, Nov. 2015.

[8] N. Nguyen-Trong, A. Piotrowski, L. Hall, and C. Fumeaux, "A frequency- and polarization-reconfigurable circular cavity antenna," *IEEE Antenna Wirel. Propag. Lett.*, vol. 16, pp. 999-1002, 2016.

[9] W. Lin and H. Wong, "Multi-polarization reconfigurable circular patch antenna with L-shaped probes," *IEEE Antenna Wirel. Propag. Lett.*, vol. 16, pp. 1549-1552, 2017.

[10] H. Wong, W. Lin, L. Huitema and E. Arnaud, "Multi-polarization reconfigurable antenna for wireless biomedical system," *IEEE Trans. Biomed. Circuits Syst.*, vol. 13, no. 3, pp. 652-660, Jun. 2017.

[11] W. Lin and H. Wong, "Wideband circular polarization reconfigurable antenna with L-shaped feeding probes," *IEEE Antennas Wirel. Propag. Lett.*, vol. 16, pp. 2114-2117, 2017.

[12] B. Li, S.-W. Liao, and Q. Xue, "Omnidirectional circularly polarized antenna combining monopole and loop radiators," *IEEE Antennas Wirel. Propag. Lett.*, vol. 12, pp. 607–610, 2013.
[13] Y. Yu, Z. Shen and S. He, "Compact omnidirectional antenna of circular polarization," *IEEE Antennas Wirel. Propag. Lett.*, vol. 11, pp. 1466–1469, 2012.
[14] W. W. Li and K. W. Leung, "Omnidirectional circularly polarized dielectric resonator antenna with top-loaded Alford loop for pattern diversity design," *IEEE Trans. Antennas Propag.*, vol. 61, no. 8, pp. 4246-4256, Aug. 2013.
[15] J. Shi, X. Wu, X. Qing, and Z. N. Chen, "An omnidirectional circularly polarized antenna array," *IEEE Trans. Antennas Propag.*, vol. 64, no. 2, pp. 578-581, Feb. 2016.
[16] H. Nakano, R. Satake, and J. Yamauchi, "Horizontally polarized, omni-directional antenna with a single feed," in *Proc. IEEE Int. Conf. Wireless Information Technology and Systems* (ICWITS), Honolulu, HI, Oct. 2010, pp. 1–4.
[17] X. Quan, R. Li, and M. M. Tentzeris, "A broadband omnidirectional circularly polarized antenna," *IEEE Trans. Antennas Propag.*, vol. 61, no. 5, pp. 2363-2370, May 2013.
[18] Y. M. Pan, S. Y. Zheng, and B. J. Hu, "Wideband and low-profile omnidirectional circularly polarized patch antenna," *IEEE Trans. Antennas Propag.*, vol. 62, no. 8, pp. 4347-4351, Aug. 2014.
[19] Y. M. Pan and K. W. Leung, "Wideband omnidirectional circularly polarized dielectric resonator antenna with parasitic strips," *IEEE Trans. Antennas Propag.*, vol. 60, no. 6, pp. 2992-2997, Jun. 2012.
[20] J. Liu, Y. Li, Z. Liang and Y. Long, "A planar quasi-magnetic-electric circularly polarized antenna," *IEEE Trans. Antennas Propag.*, vol. 64, no. 6, pp. 2108-2114, Jun. 2016.
[21] J. Wu and K. Sarabandi, "Compact omnidirectional circularly polarized antenna," *IEEE Trans. Antennas Propag.*, vol. 65, no. 4, pp. 1550-1557, Apr. 2017.
[22] Y.-M. Pan and K. W. Leung, "Wideband circularly polarized dielectric bird-nest antenna with conical radiation pattern," *IEEE Trans. Antennas Propag.*, vol. 61, no. 2, pp. 563-570, Feb. 2013.
[23] J. M. Fernandez, J. L. Masa-Campos, and M. Sierra-Perez, "Circularly polarized omnidirectional millimeter wave monopole with parasitic strip elements," *Microw. Opt. Technol. Lett.*, vol. 49, no. 3, pp. 664–668, Mar. 2007.
[24] P. K. Verma, R. Kumar and M. Signh, "Ka-band circularly polarized omnidirectional antenna for wide elevation coverage," *Elec. Lett.*, vol. 50, no. 22, pp. 1563-1564, Oct. 2014.
[25] K. M. Luk and H. Wong, "A new wideband unidirectional antenna element," *Int. J. Microw. Opt. Technol.*, vol. 1, no. 1, pp. 35–44, Jun. 2006.
[26] K. M. Luk and H. Wong, "A complementary wideband antenna," U.S. Patent No. 7843389 B2, Mar. 10, 2006.
[27] K. M. Luk and B. Wu, "The magnetoelectric dipole: A wideband antenna for base stations in mobile communications," *Proc. IEEE*, vol. 100, no. 7, pp. 2297–2307, Jul. 2012.
[28] A. Dadgarpour, M. Sharifi Sorkherizi and A. Kishk, "High efficient circularly polarized magneto-electric dipole antenna for 5G applications using dual-polarized split-Ring resonator lens," *IEEE Trans. Antennas Propag.*, vol. 65, no. 8, pp. 4263-4267, Aug. 2017.
[29] M. C. Tang, T. Shi and R. W. Ziolkowski, "A study of 28 GHz, planar, multi-layered, electrically small, broadside radiating, Huygens source antennas," *IEEE Trans. Antennas Propag.*, in process of publication, DOI: 10.1109/TAP.2017.2700888.
[30] T. Niemi, P. Alitalo, A. O. Karilainen, and S. A. Tretyakov, "Electrically small Huygens source antenna for linear polarisation," *IET Microw. Antennas Propag.*, vol. 6, no. 7, pp. 735–739, 2012.
[31] P. Alitalo, A. O. Karilainen, T. Niemi, C. R. Simovski, and S. A. Tretyakov, "Design and realization of an electrically small Huygens source for circular polarisation," *IET Microw. Antennas Propag.*, vol. 5, no. 7, pp. 783–789, 2011.
[32] P. Jin and R. W. Ziolkowski, "Metamaterial-inspired, electrically small Huygens sources," *IEEE Antennas Wirel. Propag. Lett.*, vol. 9, pp. 501–505, 2010.
[33] R. W. Ziolkowski, "Low profile, broadside radiating, electrically small Huygens source antennas," *IEEE Access*, vol. 3, pp. 2644-2651, Dec. 2015.
[34] M. C. Tang, H. Wang and R. W. Ziolkowski, "Design and testing of simple, electrically small, low-profile, Huygens source antennas with broadside radiation performance," *IEEE Trans. Antennas Propag.*, vol. 64, no. 11, pp. 4607–4617, Nov. 2016.
[35] M. C. Tang, T. Shi, and R. W. Ziolkowski, "Electrically small, broadside radiating Huygens source antenna augmented with internal non-Foster elements to increase its bandwidth," *IEEE Antennas Wirel. Propag. Lett.*, vol. 16, pp. 712-715, 2017.
[36] C. A. Balanis, 3rd Ed., *Antenna Theory*. New York: John Wiley & Sons, 2005.

Wei LIN received his PhD degree in Electronic Engineering from City University of Hong Kong, Hong Kong SAR in August 2016. He received the Master and Bachelor degrees, both in Electronic Engineering, at the South China University of Technology, Guangzhou, China in July 2012 and July 2009, respectively. He worked as a Research Associate at the Nanyang Technological University, Singapore from August 2012 to August 2013.

He is currently a postdoc research fellow with the Global Big Data Technologies Centre, University of Technology Sydney, Ultimo NSW, Australia. Dr. Lin was awarded the Outstanding Master Thesis Award from South China University of Technology in 2013. He received the Young Scientist Award at the IEEE Region 10 conference (TENCON) in December 2015 and a Talent Development Scholarship from the Hong Kong SAR Government in July 2016. His research interests include the designs of reconfigurable antennas, HF antennas, satellite antennas, millimeter wave antennas, terahertz devices, and their applications.

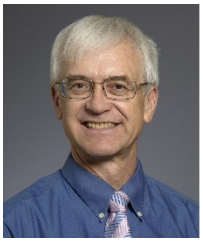

Richard W. Ziolkowski received the B.Sc. (magna cum laude) degree (Hons.) in physics from Brown University, Providence, RI, USA, in 1974; the M.S. and Ph.D. degrees in physics from the University of Illinois at Urbana-Champaign, Urbana, IL, USA, in 1975 and 1980, respectively; and the Honorary Doctorate degree from the Technical University of Denmark, Kongens Lyngby, Denmark in 2012.

He is currently a Distinguished Professor with the University of Technology Sydney, Global Big Data Technologies Centre, Ultimo NSW, Australia. He is also a Litton Industries John M. Leonis Distinguished Professor with the Department of Electrical and Computer Engineering and a Professor with the College of Optical Sciences at The University of Arizona. He was the Computational Electronics and Electromagnetics Thrust Area Leader with the Lawrence Livermore National Laboratory, Engineering Research Division, before joining The University of Arizona, Tucson, AZ, USA, in 1990. He was the Australian DSTO Fulbright Distinguished Chair in Advanced Science and Technology from 2014-2015. He was a 2014 Thomas-Reuters Highly Cited Researcher. His current research interests include the application of new mathematical and numerical methods to linear and nonlinear problems dealing with the interaction of electromagnetic and acoustic waves with complex linear and nonlinear media, as well as metamaterials, metamaterial-inspired structures, and applications-specific configurations.

Prof. Ziolkowski is a Fellow of the Optical Society of America (OSA, 2006), and of the American Physical Society (APS, 2016). He served as the President of the IEEE Antennas and Propagation Society in 2005. He is also actively involved with the URSI, OSA and SPIE professional societies.

Thomas C. Baum received his B.Eng in Aerospace Engineering (Hons.) at RMIT University in 2009. He completed his PhD. in electrical engineering for RMIT University in 2014.

In 2015, he became a research fellow at RMIT University working on a variety of microwave related research areas including conformal load bearing antenna structures, coherent Doppler tomography and dielectric material characterization. In 2017 he joined the Australian Department of Defence – Defence Science and Technology (DST) as part of the Aerospace Composite Technologies group within the Aerospace Division. His interests lie in novel antenna designs, radar systems, radar absorbing applications, scattering phenomena, microwave imaging, and material characterization.